Interpreting the Paramagnetic NMR Spectra of Potential Ru(III) Metallodrugs: Synergy between Experiment and Relativistic DFT Calculations

Jan Novotný,[†] Martin Sojka,[†,‡] Stanislav Komorovsky,[§] Marek Nečas,[†,‡] and Radek Marek*[,†,‡]

[†]CEITEC − Central European Institute of Technology, Masaryk University, Kamenice 5, CZ − 62500 Brno, Czech Republic

[‡]Department of Chemistry, Faculty of Science, Masaryk University, Kamenice 5, CZ − 62500 Brno, Czech Republic

[§]Centre for Theoretical and Computational Chemistry, Department of Chemistry, UiT − The Arctic University of Norway, N-9037 Tromsø, Norway

S *Supporting Information*

ABSTRACT: Ruthenium-based compounds are potential candidates for use as anticancer metallodrugs. The central ruthenium atom can be in the oxidation state +2 (e.g., RAPTA, RAED) or +3 (e.g., NAMI, KP). In this study we focus on paramagnetic NAMI analogs of a general structure $[\text{4-R-pyH}]^+\textit{trans}\text{-}[\text{Ru}^{III}\text{Cl}_4(\text{DMSO})(\text{4-R-py})]^-$, where 4-R-py stands for a 4-substituted pyridine. As paramagnetic systems are generally considered difficult to characterize in detail by NMR spectroscopy, we performed a systematic structural and methodological NMR study of complexes containing variously substituted pyridines. The effect of the paramagnetic nature of these complexes on the ^{1}H and ^{13}C NMR chemical shifts was systematically investigated by temperature-dependent NMR experiments and density-functional theory (DFT) calculations. To understand the electronic factors influencing the orbital (δ^{orb}, temperature-independent) and paramagnetic (δ^{para}, temperature-dependent) contributions to the total NMR chemical shifts, a relativistic two-component DFT approach was used. The paramagnetic contributions to the ^{13}C NMR chemical shifts are correlated with the distribution of spin density in the ligand moiety and the ^{13}C isotropic hyperfine coupling constants, $A_{\text{iso}}(^{13}\text{C})$, for the individual carbon atoms. To analyze the mechanism of spin distribution in the ligand, the contributions of molecular spin−orbitals (MSOs) to the hyperfine coupling constants and the spatial distribution of the z-component of the spin density in the MSOs calculated at the relativistic four-component DFT level are discussed and rationalized. The significant effects of the substituent and the solvent on δ^{para}, particularly the contact contribution, are demonstrated. This work should contribute to further understanding of the link between the electronic structure and the NMR chemical shifts in open-shell systems, including the ruthenium-based metallodrugs investigated in this account.
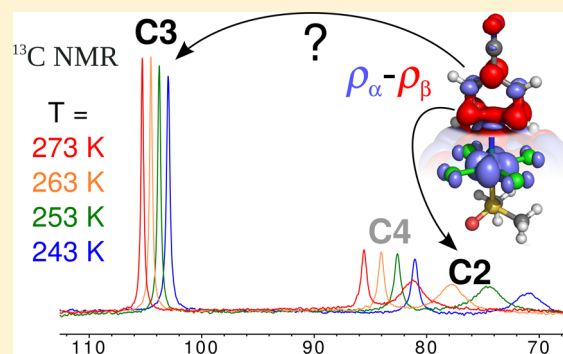
1. INTRODUCTION

Anticancer metallodrugs were introduced following the discovery of the biological properties of cisplatin reported by Rosenberg et al. in 1965.[1] Since then, many chemists have devoted great efforts to developing more effective analogs with selective modes of action and reduced undesirable side effects.[2] In recent years, ruthenium-based compounds have been explored as potential alternatives to platinum-based drugs.[3,4] There are two general classes of ruthenium-based compounds, either derived from Ru^{II} (e.g., RAPTA, RAED)[5] or Ru^{III} (e.g., NAMI, Keppler-type KP),[6,7] Figure 1. RAPTA, a representative of the Ru^{II}-based systems containing aromatic and hetero-adamantane ligands, is inactive against primary tumors but effective at reducing metastases.[8] NAMI, a representative of the Ru^{III}-based compounds, contains DMSO and a nitrogen heterocyclic ligand (imidazole) in the axial positions, whereas the equatorial positions of this octahedral complex are occupied by chlorides. This compound is active against metastases and solid tumors and

has entered the second phase of clinical trials.[9,10] It should be mentioned that NAMI is considered to be a prodrug that is converted to an active drug form by hydrolysis[11] and Ru^{III} → Ru^{II} reduction.[12]

The design and development of new Ru^{III} compounds is an active field of research involving contributions by chemists, biochemists, pharmacists, and medical doctors. Considering the indispensable role of NMR spectroscopy in characterizing the chemical structures of new compounds, Ru^{III} complexes are NMR troublemakers. Their "unfavorable" NMR properties stem from the presence of an unpaired electron (residing mainly in the ruthenium 4d shell), which induces a fast nuclear spin relaxation that results in the broadening of lines of the NMR signals. At the same time, however, the paramagnetic center induces an additional paramagnetic shift for the light atoms of the ligand.
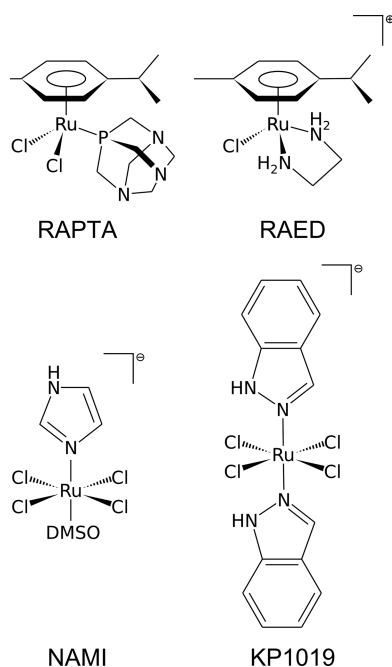
Figure 1. Structures of RAPTA, RAED, NAMI, and KP1019.

Generally, the paramagnetic contribution to the NMR shift (δ^{para}) is responsible for very broad NMR spectral windows amounting to hundreds of ppm for ^1H, and even more than a thousand ppm for heavier ligand atoms such as ^{13}C or ^{15}N.[13] These two factors, the resonance shift and the line broadening, severely hamper the observation and interpretation of the NMR spectra of paramagnetic compounds. However, the increasing predictive and interpretative power of quantum chemical calculations is gradually changing this picture. Synergy between the experimental and theoretical results enables the identification and interpretation of the NMR resonances in unusual spectral regions and of extremely broad nature.

The experimental NMR techniques applied in the field of paramagnetic systems, including biomacromolecules, have been reviewed several times.[13–16] For small molecules, the NMR data can be extracted directly from the corresponding 1D NMR spectra measured at various temperatures (T). Subsequently, the temperature-independent (orbital) and temperature-dependent (paramagnetic) contributions are determined from a Curie plot: NMR chemical shifts versus reciprocal absolute temperature ($1/T$).[17,18] It should be mentioned that the monotonic dependence in the Curie plots is obtained only for systems obeying the Curie law, i.e., for doublet or higher multiplet systems when the zero-field splitting effects are negligible.[19] It is well-known that for systems with non-negligible zero-field splitting the NMR temperature dependence becomes more complicated.[20,21]

Traditionally, the paramagnetic NMR effects have been divided into contact and pseudocontact contributions. For transition-metal complexes, the contact contribution typically vanishes relatively quickly as the number of chemical bonds from the paramagnetic metal center, for which the spin density is rather localized in the metal d-orbitals, increases. The contact contribution arises as interplay between the spin density distributed toward the ligand atoms and the Fermi-contact (FC) interaction. Because of the local nature of the FC operator, the contact contribution strongly depends on the details of the electronic structure. In contrast, the pseudocontact contribution is related to the spin-dipolar mechanism of interaction between the electron and nuclear spins and follows an inverse distance dependence ($1/r^3$).

This dependence on orientation and distance has long been used as a structural restraint in determining biomolecular structures.[16]

The development of theoretical approaches used to calculate the NMR properties of paramagnetic transition-metal systems has been discussed in a series of papers,[22–24] and it has recently been applied to systems with more than doublet multiplicity.[25–27] The common approach in calculation of the paramagnetic NMR shifts is to use EPR parameters as intermediate quantities, although in principle the theory developed by Van den Heuvel and Soncini[22] does not require it. This has been demonstrated in a recent study by Gendron et al.,[25] where the authors avoided the use of EPR parameters entirely. Currently, the computational approaches to applications in inorganic and bioinorganic chemistry and to biomolecules rely mostly on density-functional theory (DFT). For example, methods for calculating the electron paramagnetic resonance (EPR) parameters in doublet systems and NMR chemical shifts in diamagnetic systems are implemented in the ADF program using a two-component zeroth-order regular approximation (ZORA)[28] approach. Such an approach has also been used to calculate the NMR chemical shifts in some paramagnetic ruthenium(III) complexes, including NAMI.[28–31] Recently, a relativistic four-component DFT approach has been used to calculate the pNMR spectra of doublet systems (including an application on NAMI).[32] Reference 33 exemplifies the recent reviews of the NMR calculations for paramagnetic substances.

In this study, we designed and prepared several pyridine-based Ru^{III} systems (Figure 2) to investigate and interpret the
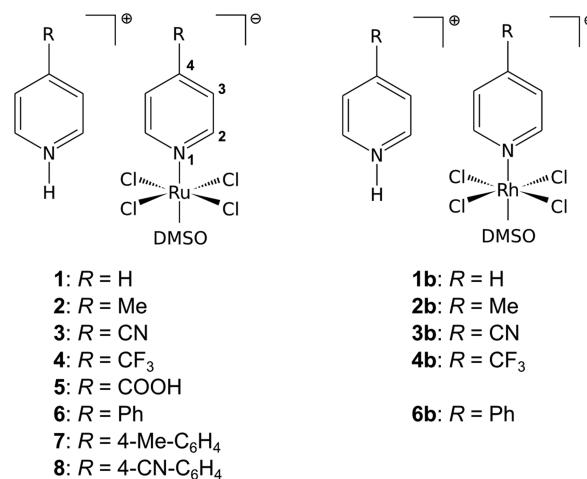

1: R = H
2: R = Me
3: R = CN
4: R = CF$_3$
5: R = COOH
6: R = Ph
7: R = 4-Me-C$_6$H$_4$
8: R = 4-CN-C$_6$H$_4$

1b: R = H
2b: R = Me
3b: R = CN
4b: R = CF$_3$

6b: R = Ph

Figure 2. Structure and atom numbering scheme for Ru^{III}-based compounds **1**–**8** and their Rh^{III} analogs **1b**–**4b**, **6b**.

NMR properties of the individual hydrogen and carbon atoms as well as the details of the propagation of the electronic effects in ligands. The compounds **1**–**8** differ in the nature of the *para*-substituent on the pyridine ligand found in the *trans*-position to DMSO, basically in the donor/acceptor properties of the R substituent (e.g., a Me vs a CN group in **2** and **3**), and in an extension of the conjugated aromatic system (compounds **6**–**8**).

Combining the experimental NMR measurements at various temperatures with relativistic DFT calculations of the NMR chemical shifts enables us to understand the electronic structure of the Ru^{III} complexes and its relation to the observable NMR characteristics. In this paper we demonstrate and interpret a link between the paramagnetic contributions to the NMR chemical shifts and the distribution of spin density in the axial pyridine-derived ligands. The two-component ZORA approach,

as implemented in the ADF program,[34] is used to correlate the experimental NMR chemical shifts with the DFT-calculated values and to investigate the electronic factors responsible for the propagation of spin density to the ligand moiety. The effects of solvent on the DFT-calculated paramagnetic contributions to the NMR chemical shifts are also investigated. The four-component DKS approach, as implemented in the ReSpect code,[35] is used to estimate the mechanism of the hyperfine interaction for selected ligand atoms. Finally, the electronic effects of the *para*-substituents on the pyridine ring on the NMR chemical shifts are rationalized.

2. METHODS

2.1. Synthesis. *Materials.* The starting compounds $RuCl_3 \cdot xH_2O$, $RhCl_3 \cdot xH_2O$, pyridine, 4-methylpyridine, 4-pyridinecarbonitrile, 4-(trifluoromethyl)pyridine, 4-phenylpyridine, pyridine-4-carboxylic acid, *p*-tolylboronic acid, (4-cyanophenyl)boronic acid, triphenylphosphine, palladium(II) acetate, and sodium hydrogen carbonate were used as obtained from our suppliers. The solvents in p.a. grade were used as is with no further purification unless otherwise stated. $[DMSOH]trans\text{-}[RuCl_4(DMSO)_2]$ and $[DMSOH]trans\text{-}[RhCl_4(DMSO)_2]$ were prepared according to previously reported procedures.[36,37] Similarly, (4-cyanophenyl)pyridine and *p*-tolylpyridine were prepared according to reported procedures.[38]

General Synthetic Procedure for Compounds 1–3, 5–8, 1b–3b, and 6b. Ru(III) and Rh(III) octahedral complexes with pyridine derivatives were synthesized in a manner similar to that reported by Webb and co-workers,[39] but in a slightly modified way. Finely grounded $[DMSOH]trans\text{-}[MCl_4(DMSO)_2]$ (M = Ru, Rh) (0.209 mmol) was dispersed in 6 mL of acetone. The selected pyridine derivative (0.627 mmol) was then added to the reaction mixture at room temperature and the reaction mixture turned to a clear orange-red solution. Within a few minutes a light orange solid started to separate from the solution. Each reaction was complete in 2 to 3 h. The resulting precipitate was collected

by filtration, washed with diethyl ether (3 × 3 mL) and dried *in vacuo* for 5 h.

Synthetic Procedure for 4 and 4b. $[DMSOH]trans\text{-}[MCl_4(DMSO)_2]$ (M = Ru, Rh) (0.209 mmol) was diluted in 6 mL of acetone and 4-CF$_3$-py (0.627 mmol) was added dropwise to the reaction mixture. The solution turned bright orange, but no precipitation of solid product was observed. After 2 h the reaction mixture was overlaid with diethyl ether (6 mL) and placed in a freezer for 12 h. Gleaming yellow flakes of the product were collected by filtration, washed with cold diethyl ether (2 × 1 mL) and dried *in vacuo* for 5 h.

2.2. X-ray Diffraction. Diffraction data for the present Ru(III) and Rh(III) complexes were collected on a Rigaku MicroMax-007 HF rotating anode four-circle diffractometer with Mo Kα radiation. The temperature during data collection was 120(2) K. The structures were solved by direct methods and refined by standard methods using the ShelXTL software package.[40] Crystallographic data and structural refinement parameters are listed in Table 1.

2.3. NMR Spectroscopy. The ^1H, ^{13}C, and 2D NMR spectra of Ru(III) complexes **1–8** and Rh(III) complexes **1b–4b**, **6b** were measured on a Bruker Avance III HD 700 MHz spectrometer. The NMR samples were prepared by dissolving 5–15 mg of the complex in 0.5 mL of DMF-d_7. The signals of the solvent ($\delta(^1H)$ = 8.03 ppm, $\delta(^{13}C)$ = 163.2 ppm) served to reference the temperature-dependent NMR spectra. The 2D ^1H–^{13}C chemical shift correlation spectra (HSQC, HMBC) were rather inefficient for Ru(III) complexes due to the fast spin relaxation caused by the paramagnetic center. In such cases, ^1H-coupled ^{13}C NMR spectra were used to distinguish between the NMR resonances of C–H and Cq atoms. Long-range ^1H–X chemical shift correlation experiments (namely ^1H–$^{13}C/^{15}N$ HMBC)[41] were employed to unambiguously assign the organic ligand in the Rh(III) diamagnetic analogs and the atoms of phenyl-pyridine derivatives more distant from the ruthenium center.

2.4. Quantum Chemical Calculations. *Geometry.* The structures were optimized using density-functional theory (DFT) with the PBE0 functional[42,43] and the def2-TZVPP[44] basis set for all atoms (if not otherwise stated), with corresponding relativistic effective core potentials (def2-ECPs)[45] for the metal centers (ECP substituting

Table 1. Crystallographic Data for Ruthenium Complexes 3, 4, and 7 and Rhodium Complexes 2b–4b

	3	4	7	2b	3b	4b
CCDC No	1465347	1465348	1465349	1465350	1465351	1465352
chemical formula	$C_{14}H_{15}Cl_4N_4ORuS$	$C_{14}H_{15}Cl_4F_6N_2ORuS$	$C_{26.50}H_{30}Cl_5N_2ORuS$	$C_{14}H_{21}Cl_4N_2ORhS$	$C_{14}H_{15}Cl_4N_4ORhS$	$C_{14}H_{15}Cl_4F_6N_2ORhS$
formula weight	530.23	616.21	702.90	510.10	532.07	618.05
crystal system	monoclinic	monoclinic	triclinic	triclinic	monoclinic	monoclinic
space group	$P2_1/n$	$P2_1/n$	$P\bar{1}$	$P\bar{1}$	$P2_1/n$	$P2_1/n$
a (Å)	7.1525(4)	7.8013(2)	15.1499(3)	9.2004(1)	7.1887(2)	7.7976(4)
b (Å)	23.0424(18)	10.8212(4)	17.3913(3)	15.2100(3)	22.9114(7)	10.7641(6)
c (Å)	11.8290(9)	25.0170(8)	23.9791(4)	15.6366(2)	11.8104(3)	25.0618(16)
α (deg)	90	90	76.679(2)	71.257(1)	90	90
β (deg)	90.688(6)	95.030(2)	89.978(2)	73.832(1)	90.630(3)	95.151(5)
γ (deg)	90	90	77.344(2)	72.534(2)	90	90
V (Å^3)	1949.4(2)	2103.79(12)	5990.2(2)	1936.04(6)	1945.08(10)	2095.0(2)
Z	4	4	8	4	4	4
$D_{calcd.}$ (g cm^{-3})	1.807	1.946	1.559	1.750	1.817	1.959
F (000)	1052	1212	2848	1024	1056	1216
μ (mm^{-1})	1.47	1.41	1.06	1.55	1.55	1.49
measured/unique reflections	7115/7115^a	13381/4005	31596/31596^a	24372/7342	12320/3685	11902/3982
data/parameters	7115/229	4005/301	31596/1388	7342/423	3685/228	3982/301
R_1/wR_2 [I > 2σ(I)]	0.0709/0.2195	0.0300/0.0745	0.0455/0.1381	0.0216/0.0540	0.0412/0.1105	0.0779/0.2138
R_1/wR_2 [all data]	0.0768/0.2295	0.0376/0.0788	0.0575/0.1462	0.0226/0.0547	0.0499/0.1164	0.0822/0.2171
GoF	1.035	1.032	1.014	1.053	1.079	1.103
$\Delta\rho_{max}/\Delta\rho_{min}$ (e Å^{-3})	1.67/−2.65	0.68/−1.23	2.08/−1.19	0.70/−0.57	1.05/−0.85	4.02/−1.21

^{a}The crystals were non-merohedrally twinned, and unmerged data were used for the refinement.

28 electrons for Ru and Rh), as implemented in the Turbomole 6.03 program.[46] The structures were optimized either in a vacuum or by using the COSMO (Conductor-like Screening Model)[47] solvent model (for Cartesian coordinates, see Supporting Information). All calculations were performed using an m5 integration grid with the following convergence criteria: 10^{-6} for the energy change and 10^{-3} for the geometry gradient. We used an approach calibrated in our previous studies of octahedral and square-planar transition-metal complexes.[48,49]

NMR Chemical Shifts, EPR Parameters. The NMR shielding constants were calculated using the methods of density-functional theory (DFT) mentioned below. The systematic offsets of the DFT methods used in calculating the NMR chemical shifts were reduced by using benzene (in benzene)[48–52] as a secondary reference relative to TMS: $\delta_{ref} = 7.15$ ppm for ^{1}H and $\delta_{ref} = 127.8$ ppm for ^{13}C.

$$\delta_i = \sigma_{ref} - \sigma_i + \delta_{ref} \qquad (1)$$

where δ_i is the NMR chemical shift of interest, σ_{ref} and σ_i are the NMR shielding constants of particular atoms in the secondary reference (benzene) and the molecule being investigated, respectively.

The presence of a counterion was neglected in our production calculations (the effect of the presence and nature of the countercation in the calculations on the NMR chemical shifts was estimated as presented in Supporting Information) of the total NMR chemical shifts (δ^{tot}) composed of orbital (δ^{orb}, temperature-independent) and paramagnetic (δ^{para}, temperature-dependent) contributions.

$$\delta^{tot} = \delta^{orb} + \delta^{para} \qquad (2)$$

The value of the *temperature-dependent* paramagnetic shift (δ^{para}) was obtained as the sum of the traditional contact (δ^{con}) and pseudo-contact (δ^{pc}) terms based on the following eqs 3 and 4:

$$\delta_M^{con} = \frac{\mu_e S(S+1)}{3kT\gamma_M} g_{iso} A_{iso}(M) \qquad (3)$$

$$\delta_M^{pc} = \frac{\mu_e S(S+1)}{9kT\gamma_M} \mathrm{Tr}[\mathbf{g}_{ani}\mathbf{A}_{dip}(M)] \qquad (4)$$

A thorough discussion of eqs 3 and 4 can be found in reference 32 and the references cited therein. For the present purpose, analysis of their dependence on the isotropic and anisotropic contributions to tensors **g** and **A** will be sufficient. Note that eqs 3 and 4 hold only for systems with negligible zero-field splitting (ZFS) effects. For the full theory, which also incorporates ZFS effects, see refs 22, 24.

Two-Component DFT Approach to NMR and EPR Parameters. The NMR shielding constants along with the EPR parameters were calculated by using the ADF program ADF2014.[53] The calculations were performed at the 2c (SO-ZORA) level,[54,55] using the PBE0 functional,[56,57] the TZ2P basis set,[58] and the COSMO solvent model,[47] as implemented in the ADF program. The relativistic unrestricted calculations used collinear approximation.[59] Note that the methodology applied in this work for the calculation of EPR parameters cannot be used for systems with degenerate highest occupied one-electron energy. However, because the method used includes spin–orbit coupling variationally, the number of such cases is reduced compared to the SO-free approach. Still this degenerate situation can appear for systems with high spatial symmetry (absent for the systems investigated in this work). As the current two-component implementation of the NMR calculations in the ADF program is limited to closed-shell systems, diamagnetic Ru(II) analogs were employed to calculate the orbital contributions (δ^{orb}) to the total NMR chemical shifts and compared with their diamagnetic Rh(III) counterparts.

The performance of the method used in this work was evaluated by calculating the deviations of theoretical NMR chemical shifts from the experimental values (^{1}H NMR in Figure S1 and ^{13}C NMR in Figure S2 in Supporting Information). The calculated mean absolute error (MAE) is about 1.13 ppm for the total ^{1}H NMR chemical shifts (MAE = 0.76 ppm for δ^{orb} and 0.64 ppm for δ^{para}) and about 6.2 ppm for the total ^{13}C NMR chemical shifts (MAE = 3.6 ppm for δ^{orb} and 4.0 ppm for δ^{para}).

The main source of deviations for ^{1}H NMR spectra is atom H2, which is also very sensitive to solvent effects (see Figure S3). The correct treatment of this atom would probably require inclusion of the explicit solvent and dynamics in the NMR chemical shift calculations. However, the implicit solvent model does a very good job for the other atoms as expressed by the MAE values for ^{1}H (5.06 ppm for vacuum vs 1.13 ppm for COSMO) and ^{13}C (23.4 ppm for vacuum vs 6.2 ppm for COSMO) NMR data, see Figure S3. The effects of solvent, level of relativistic approximation, and amount of exact-exchange admixture in the PBE0 functional on the H2, H3 and C2, C3 NMR chemical shifts for compound **3** are summarized in Figure S4. In addition, we evaluated the effects of the presence and nature of the counterion (in optimized geometry for Na$^+$ and X-ray derived geometry for the organic cation) on the calculated NMR chemical shifts (Figure S5) for compound **2**. The presence of a counterion alters the total ^{1}H (^{13}C) NMR chemical shifts by about 1 ppm (2 ppm), solvent by 8 ppm (30 ppm), level of relativity by 3 ppm (20 ppm), and amount of exact-exchange admixture in the PBE0 functional (0 vs 25%) by 2 ppm (60 ppm). Some authors ascribe the latter effect partly to the delocalization error of the GGA functionals.[60–62] To check the effect of the exact-exchange admixture in the PBE0 functional on the delocalization, we plot the spin density for compound **3** at the PBE and PBE0 levels (Figure S6 in Supporting Information). As expected, the plots indicate a slightly larger spin delocalization to the pyridine ligand at the PBE level.

The spatial distribution of total spin density and spin populations for individual ligand atoms in the ruthenium complexes discussed in the main text were calculated at the scalar-relativistic (ZORA/PBE0/TZ2P) level, 1c, either in a vacuum or by using the COSMO solvent model (DMF).

Four-Component DFT Approach to EPR Parameters. The EPR parameters were calculated by using the relativistic DFT program ReSpect (version 3.4.2).[35] All calculations were performed at the four-component Dirac–Kohn–Sham (DKS) level of theory[63–65] using a upcJ-1[66] basis set for the light atoms and a Dyall's-vdz[67] basis set for Ru (smaller basis sets were used to simplify the analysis). The PBE0 functional[56,57] was employed to calculate the EPR parameters (g-tensors and ligand hyperfine coupling tensors, A-tensors). The contributions from molecular spin–orbitals (MSOs) to the A-tensors as well as the spatial distribution of the z-component of the 4c spin density for the individual MSO (see Section 3.5) were analyzed to interpret the electronic factors influencing the paramagnetic contributions to the NMR chemical shifts. The expression for the contributions of the individual MSOs to the four-component A-tensor can be found as eq 16 in reference 65.

3. RESULTS AND DISCUSSION

3.1. Molecular Geometry: X-ray Diffraction and DFT Calculations. The desired Ru(III) and Rh(III) complexes were obtained in high yields as pale to bright orange powders stable in air. The complexes were recrystallized from mixtures of dichloromethane with hexane or DMF with diethyl ether. Generally, we used somewhat lower molar ratios than those reported elsewhere,[39,68] because we had observed multiple substitution at the central metal atom and lower yields when we followed the published procedures. The crystal structures obtained in this study (see Table 1), as well as those reported previously,[69–71,39] have been used as references for our DFT optimizations of the molecular structures. The Ru–N, Ru–S, Rh–N, and Rh–S interatomic distances are summarized in Table 2 and the molecular structure of compound **7** determined by using X-ray diffraction is shown in Figure 3.

To optimize the structures we used a hybrid PBE0 functional which had previously been found to perform very well in optimizing the geometry of octahedral[48] and square-planar[49] transition-metal complexes.[72,73] The def2-TZVPP basis set (with the corresponding relativistic effective-core potential, def2-ECP,

Table 2. Ru−N, Ru−S, Rh−N, and Rh−S Interatomic Distances for Ruthenium Complexes 1−4 and 6 and Their Rhodium Analogs 1b−4b and 6b As Determined by X-ray Diffraction and As Calculated by Density Functional Theory (PBE0/def2-TZVPP/ECP/COSMO)[a]

	X-ray				DFT			
	Ru−N	Ru−S	Rh−N	Rh−S	Ru−N	Ru−S	Rh−N	Rh−S
1[b]/**1b**	211.7	229.5	−[c]	−[c]	211.5	229.1	208.1	229.3
2[b]/**2b**	211.3	229.1	208.1	227.4	211.4[d]	229.2[d]	207.8	229.4
3/**3b**	212.8	227.8	209.7	225.8	211.0[e]	229.2[e]	208.2[f]	228.8[f]
4/**4b**	211.8	227.9	208.5	226.5	211.5	229.1	208.4	228.8
6/**6b**	211.3	228.3	−[c]	−[c]	211.3	229.2	207.8	229.2

[a]All distances are in picometers (pm). [b]Reference 39. [c]Data not available. [d]For optimization with the alternative def2-QZVPP basis set: 210.7 pm (Ru−N) and 227.8 pm (Ru−S). [e]For optimization with the alternative def2-QZVPP basis set: 210.4 pm (Ru−N) and 227.9 pm (Ru−S). [f]For optimization with the alternative def2-QZVPP basis set: 208.0 pm (Rh−N) and 227.4 pm (Rh−S).
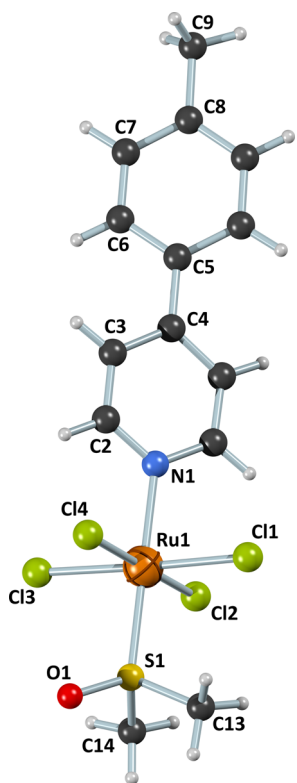

Figure 3. Molecular structure of compound **7** as determined by X-ray diffraction with atom numbering scheme (the cation is omitted for clarity). For crystallographic data, see Table 1.

for a ruthenium or rhodium atom) was used for all the atoms as an excellent compromise between the requirements for accuracy and computational speed.[48,49] Although the DFT optimizations were performed using an implicit model of solvent (COSMO), Table 2 demonstrates very good agreement between the interatomic distances determined by X-ray diffraction analysis and those calculated by DFT with relativistic ECP. Generally, the experimental X-ray Ru−N distance ranges between 211 and 213 pm and is reproduced perfectly by the values (211−212 pm) calculated using DFT. The differences between the experimental and the calculated values are somewhat larger for the Ru−S bond. This rather weak bond is known to be very sensitive to the selection of the density functional and the basis set.[48,49] The Ru−S distances are approximately 229 pm for the structures optimized by using the def2-TZVPP basis set, but get somewhat shorter (227−228 pm) for the structures optimized by using the larger def2-QZVPP basis set, almost matching the

experimental values (227−229 pm, Table 2). As these basis-set-related structural changes (Table S1) result in rather marginal differences in the calculated NMR parameters (Table S2, shielding difference for ^{1}H ∼ 0.15 ppm, for ^{13}C ∼ 1.5 ppm), the def2-TZVPP basis set was used to optimize geometry, see Section 3.3.

3.2. Effects of Temperature on the Experimental ^{1}H and ^{13}C NMR Chemical Shifts: Orbital and Paramagnetic Contributions. The experimental NMR chemical shifts of the ruthenium complexes (for ^{1}H and ^{13}C NMR chemical shifts, see Table 3 and Table 4, respectively) were assigned based on the chemical shift ranges, resonance broadening, temperature changes, and the correlation of individual chemical shifts with those for the diamagnetic rhodium analogs as well as the values calculated using DFT, see Section 3.3.

The ^{1}H and ^{13}C NMR spectra of ruthenium complexes **1−8** were typically measured in the temperature range 233−323 K. An example of the ^{1}H and ^{13}C NMR spectra of complex **3** plotted at three selected temperatures is shown in Figure 4, parts a and b, respectively. It is clear from these plots that the paramagnetic contribution (contact and pseudocontact terms) induces additional nuclear shielding at the hydrogen and carbon atoms at lower temperatures (cf. Section 3.3 and 3.5). The only exception in Figure 4 is the carbon atom of the CN group, which is slightly deshielded (i.e., shifted to a higher frequency) at lower temperature. The relationship between the shielding/deshielding effects of the paramagnetic (predominantly contact) term and the electronic structure is discussed in Sections 3.3 and 3.5.

Because the systems investigated in this work are of a doublet nature, the *temperature-independent* orbital shifts (δ^{orb}) and *temperature-dependent* paramagnetic shifts (δ^{para}) can be estimated from $1/T$ plots. An example of the $1/T$ plot for compound **3** is shown in Figure 5 and the rest of the $1/T$ plots can be found in Supporting Information. The precision of this analysis in determining δ^{orb} and δ^{para} is estimated to be about ±0.2 ppm and ±1 ppm for the ^{1}H and ^{13}C NMR chemical shifts, respectively. However, the deviations for atoms in very close proximity to the ruthenium center (particularly H2 and Me$_{DMSO}$) can amount to ±1 ppm and ±5 ppm for the ^{1}H and ^{13}C NMR chemical shifts, respectively. This estimated error should be taken into account when comparing the experimental and calculated NMR data in Section 3.3. The experimental total NMR chemical shifts (δ^{tot}) as well as the orbital (δ^{orb}) and paramagnetic (δ^{para}) NMR chemical shifts are summarized in Table 3 (^{1}H NMR) and Table 4 (^{13}C NMR).

To complement the signal assignment of the Ru^{III}-based complexes and to estimate the orbital contribution (δ^{orb}) in their diamagnetic analogs, selected rhodium(III) complexes were

Table 3. Total Experimental ^{1}H NMR Chemical Shifts (δ^{tot}) for Ruthenium Complexes 1−8 Measured at 293 K and Their Separation into Their Orbital (δ^{orb}, Temperature-Independent) and Paramagnetic (δ^{para}, Temperature-Dependent) Contributions^a

		1	2	3	4	5	6	7	8
compound		H	Me	CN	CF$_3$	COOH	Ph	MeC$_6$H$_4$	CNC$_6$H$_4$
Me$_{DMSO}$	δ^{orb}	+3.9	+2.7	+3.2	+3.8	+3.2	+3.2	+3.1	+4.3
	δ^{para}	−16.6	−15.5	−15.7	−16.3	−15.8	−15.9	−15.8	−16.9
	δ^{tot}	−12.7	−12.8	−12.5	−12.5	−12.6	−12.7	−12.7	−12.6
H2	δ^{orb}	+7.8	+6.6	+7.1	+7.1	+6.1	+6.2	+7.0	+8.6
	δ^{para}	−14.9	−14.0	−11.9	−12.1	−11.7	−13.0	−13.8	−14.8
	δ^{tot}	−7.1	−7.4	−4.8	−5.0	−5.6	−6.8	−6.8	−6.2
H3	δ^{orb}	+7.6	+7.4	+7.6	+7.8	+7.8	+7.5	+7.6	+7.8
	δ^{para}	−9.5	−9.4	−8.5	−8.6	−9.1	−9.0	−9.1	−9.1
	δ^{tot}	−1.9	−2.0	−0.9	−0.8	−1.3	−1.5	−1.5	−1.3
H6	δ^{orb}	–	–	–	–	–	+7.7	+7.6	+7.9
	δ^{para}	–	–	–	–	–	−1.7	−1.7	−1.6
	δ^{tot}	–	–	–	–	–	+6.0	+5.9	+6.3
H7	δ^{orb}	–	–	–	–	–	+7.6	+7.4	+7.7
	δ^{para}	–	–	–	–	–	−1.3	−1.3	−0.9
	δ^{tot}	–	–	–	–	–	+6.3	+6.1	+6.8

^{a}The NMR chemical shifts are in ppm. H4 in compound **1**: δ^{orb} = +7.4, δ^{para} = −1.6, δ^{tot} = +5.8; Me in compound **2**: δ^{orb} = +3.0, δ^{para} = −6.0, δ^{tot} = −3.0; H8 in compound **6**: δ^{orb} = +7.4, δ^{para} = −0.3, δ^{tot} = +7.1; Me in compound **7**: δ^{orb} = +2.7, δ^{para} = −1.4, δ^{tot} = +1.3.

Table 4. Total Experimental ^{13}C NMR Chemical Shifts (δ^{tot}) for Ruthenium Complexes 1−8 Measured at 293 K and Their Separation into Their Orbital (δ^{orb}, Temperature-Independent) and Paramagnetic (δ^{para}, Temperature-Dependent) Contributions^a

		1	2	3	4	5	6	7	8
compound		H	Me	CN	CF$_3$	COOH	Ph	MeC$_6$H$_4$	CNC$_6$H$_4$
Me$_{DMSO}$	δ^{orb}	+43	+45	+35	+43	+41	+33	–^{b}	–^{b}
	δ^{para}	−153	−156	−146	−153	−150	−144	–^{b}	–^{b}
	δ^{tot}	−110	−111	−111	−110	−109	−111	−110	−110
C2	δ^{orb}	+166	+162	+165	+165	+162	+161	+163	+164
	δ^{para}	−75	−72	−78	−76	−73	−72	−73	−75
	δ^{tot}	+91	+90	+87	+89	+89	+89	+90	+89
C3	δ^{orb}	+122	+123	+124	+117	+120	+121	+119	+119
	δ^{para}	−23	−25	−17	−19	−20	−24	−23	−21
	δ^{tot}	+99	+98	+107	+98	+100	+97	+96	+98
C4	δ^{orb}	+137	+152	+123	+141	+140	+152	+153	+150
	δ^{para}	−24	−27	−34	−33	−29	−29	−30	−31
	δ^{tot}	+113	+125	+89	+108	+111	+122	+123	+119
C5	δ^{orb}	–	–	–	–	–	+138	+136	+143
	δ^{para}	–	–	–	–	–	+3	+2	+4
	δ^{tot}	–	–	–	–	–	+141	+138	+147
C6	δ^{orb}	–	–	–	–	–	+129	+129	+129
	δ^{para}	–	–	–	–	–	−8	−8	−8
	δ^{tot}	–	–	–	–	–	+121	+121	+121
C7	δ^{orb}	–	–	–	–	–	+130	+124	+134
	δ^{para}	–	–	–	–	–	+1	+3	+1
	δ^{tot}	–	–	–	–	–	+131	+127	+135
C8	δ^{orb}	–	–	–	–	–	+131	+142	+115
	δ^{para}	–	–	–	–	–	−4	−5	−7
	δ^{tot}	–	–	–	–	–	+127	+137	+109
C$_{subst}$^{c}	δ^{orb}	–	+21	+117	+125	+167	–	+22	+119
	δ^{para}	–	0	+11	+4	−1	–	0	+2
	δ^{tot}	–	+21	+128	+129	+166	–	+22	+121

^{a}The NMR chemical shifts are in ppm. ^{b}Not determined because of the low S/N ratio resulting from significant signal broadening. ^{c}C$_{subst}$ stands for the carbon atom of the Me (**2** and **7**), CN (**3** and **8**), CF$_3$ (**4**), or COOH (**5**) group.

synthesized and measured (**1b−4b**, **6b**). Their NMR resonances were assigned by using ^{1}H−^{13}C and ^{1}H−^{15}N NMR chemical shift correlation experiments.[74−77] For example, portions of the

^{1}H−^{13}C gHMBC, ^{1}H−^{13}C gHSQC, and ^{1}H−^{15}N gHMBC spectra of the rhodium analog **6b** are shown in Figure S7 in Supporting Information. The experimental NMR chemical
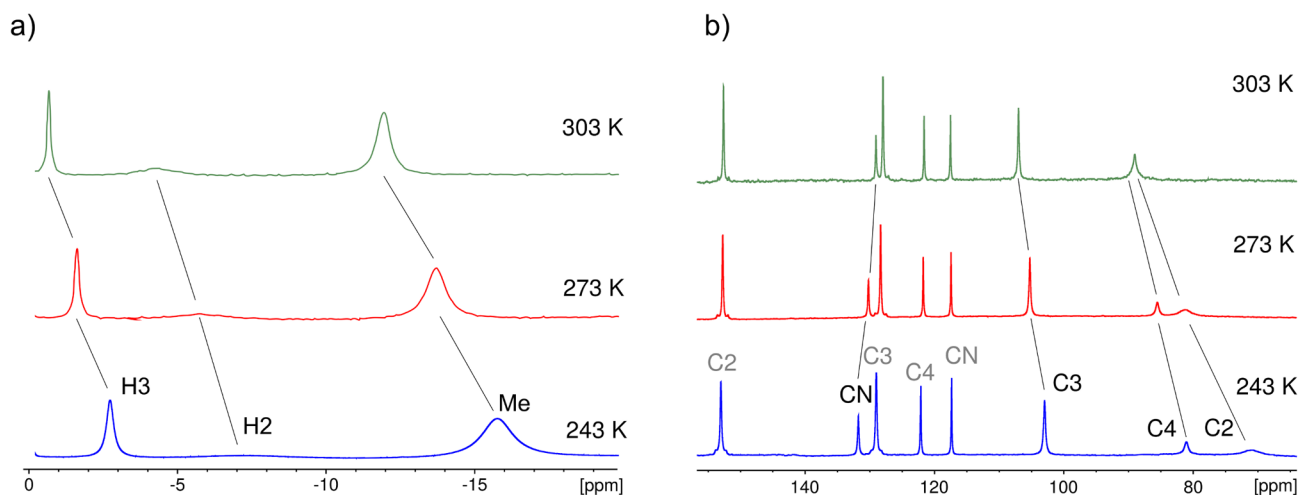
Figure 4. A portion of (a) the ^{1}H and (b) the ^{13}C NMR spectrum of compound **3** plotted for the selected temperature range 243−303 K. The ^{1}H and the ^{13}C NMR signals are assigned to individual atoms, and ^{13}C NMR signals of the countercation are shown in gray.
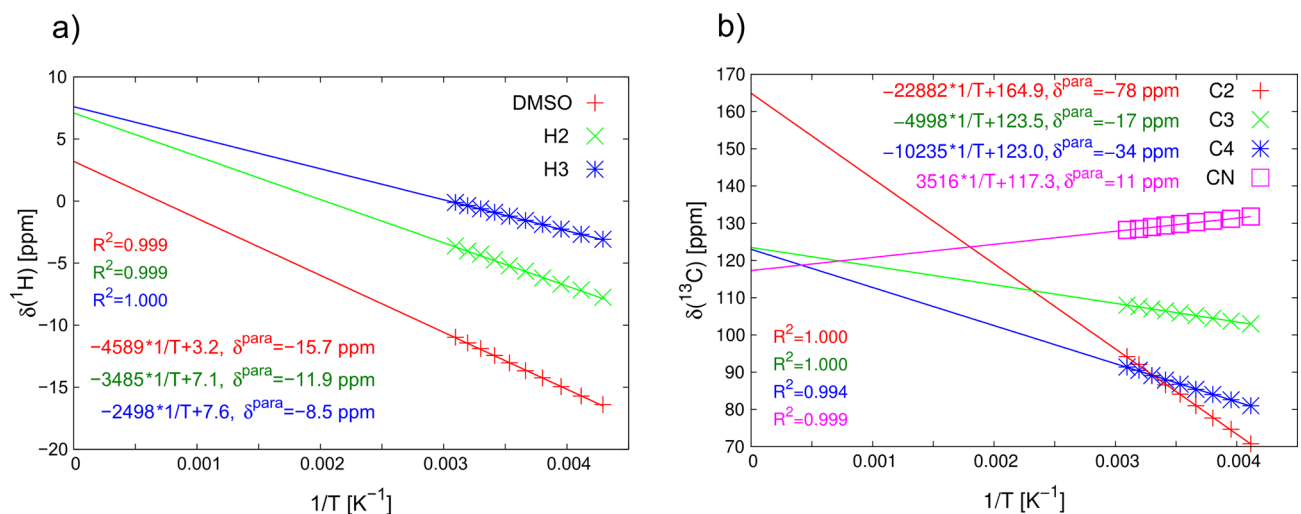

Figure 5. $1/T$ plots of (a) the ^{1}H and (b) the ^{13}C NMR chemical shifts for compound **3**. The orbital contributions (temperature independent) of the NMR chemical shifts are estimated from an extrapolation to the limit $1/T = 0$. The values of δ^{para} for individual atoms are shown for a temperature of 293 K.

shifts for rhodium complexes **1b−4b** and **6b** are summarized in Table S3 in Supporting Information.

3.3. DFT Calculations for Interpreting the Experimental Data: Paramagnetic NMR Chemical Shifts, Solvent Effects. *Method and Effects of Solvent.* The DFT calculations were performed to interpret the experimental NMR chemical shifts and to investigate the electronic factors influencing the orbital and paramagnetic contributions to the total NMR chemical shifts. The geometries of the ruthenium complexes (anions) used for the NMR chemical-shift calculations (for the effect of a countercation on the NMR chemical shifts, see Figure S5 in Supporting Information) were optimized at the PBE0/def2-TZVPP/def2-ECP level[48,49] using an implicit model of dimethylformamide solvent (COSMO), see Section 3.1. It should be noted explicitly that all the DFT calculations of the NMR parameters presented in this work were performed at the two-component relativistic level (SO-ZORA, for details, see Section 2: Methods) except the MSO analysis of A_{iso} in Section 3.5, where four-component methodology was used. Similarly, the spin density was calculated at the one-component level (ZORA) except the *z*-component of the 4c spin

density linked to the effect of exact-exchange admixture in the PBE0 (Figure S6) and the MSO analysis of A_{iso} in Section 3.5.

To calculate the NMR shielding constants, we employed the PBE0/TZ2P/SO-ZORA/COSMO approach calibrated in our previous work.[48,49] The values of the contact, pseudocontact, and orbital contributions[28,31] to the ^{1}H and ^{13}C NMR shielding constants were obtained by averaging the values for all chemically equivalent atoms. The ^{1}H and ^{13}C NMR shielding constants of benzene[50−52] were used to calculate the ^{1}H and ^{13}C NMR chemical shifts (Table 5), respectively, using the equations described in Section 2: Methods.

The solvent effects on the NMR chemical shifts were estimated as the differences between the NMR chemical shifts calculated by using an implicit solvent model and those calculated on identical structures *in vacuo*. To unambiguously distinguish the NMR signals of the counterions in the experimental NMR spectra, we also calculated the NMR chemical shifts of the corresponding protonated bases (countercations, data not shown). Selected DFT-calculated and experimental NMR data for ruthenium complexes **2** and **3** and their rhodium analogs **2b** and **3b** are summarized in Table 5 (for a full set of the

Table 5. DFT-Calculated (SO-ZORA) and Experimental ^{1}H and ^{13}C NMR Chemical Shifts (δ in ppm) for Ruthenium Complexes 2 and 3 and Their Rhodium Analogs 2b and 3b in Dimethylformamide (DMF) at 293 K^a

| | | compounds 2 and 2b | | | | | compounds 3 and 3b | | | | |
| | | 2c SO-ZORA | | | experiment | | 2c SO-ZORA | | | experiment | |
		δ_{vac}	Δ_{solv}	δ_{solv}	2 (Ru)	2b (Rh)	δ_{vac}	Δ_{solv}	δ_{solv}	3 (Ru)	3b (Rh)
H2	δ^{orb}	+9.6	−0.6	+9.0	+6.6	+9.2	+9.6	−0.3	+9.3	+7.1	+9.7
	δ^{para}	−6.1	−8.7	−14.8	−14.0	−	−0.4	−10.4	−10.8	−11.9	−
	δ^{tot}	+3.5	−9.4	−5.9	−7.4	+9.2	+9.2	−10.7	−1.5	−4.8	+9.7
H3	δ^{orb}	+5.8	+1.2	+7.0	+7.4	+7.3	+5.6	+1.7	+7.3	+7.6	+8.1
	δ^{para}	−8.9	−0.8	−9.7	−9.4	−	−10.1	+0.2	−9.9	−8.5	−
	δ^{tot}	−3.1	+0.3	−2.8	−2.0	+7.3	−4.5	+1.9	−2.6	−0.9	+8.1
C2	δ^{orb}	+161	−5	+155	+162	+156	+163	−6	+157	+165	+157
	δ^{para}	−84	+9	−75	−72	−	−99	+13	−86	−78	−
	δ^{tot}	+77	+3	+80	+90	+156	+64	+7	+71	+87	+157
C3	δ^{orb}	+113	+10	+123	+123	+125	+117	+7	+124	+124	+126
	δ^{para}	−7	−21	−28	−25	−	+18	−33	−15	−17	−
	δ^{tot}	+106	−11	+95	+98	+125	+135	−26	+109	+107	+126
C4	δ^{orb}	+130	+19	+149	+152	+152	+117	−2	+115	+123	+123
	δ^{para}	−52	+24	−28	−27	−	−87	+45	−42	−34	−
	δ^{tot}	+78	+43	+121	+125	+152	+30	+43	+73	+89	+123
C$_{subst}$	δ^{orb}	+13	0	+13	+21	+21	+130	−6	+124	+117	+118
	δ^{para}	+12	−10	+2	0	−	+59	−38	+21	+11	−
	δ^{tot}	+25	−10	+15	+21	+21	+189	−44	+145	+128	+118

^{a}For computational details, see Section 2: Methods. Mean absolute errors (MAEs): ^{1}H NMR chemical shifts for compound 2 − 1.1 ppm (1.1 for δ^{orb} and 0.7 for δ^{para}) and 3 − 2.0 ppm (0.9 for δ^{orb} and 1.2 for δ^{para}); ^{13}C NMR chemical shifts for compound 2 − 6.7 ppm (4.2 for δ^{orb} and 3.1 for δ^{para}) and 3 − 8.9 ppm (6.2 for δ^{orb} and 8.1 for δ^{para}).

experimental NMR chemical shifts for ruthenium complexes, see Table 3 and Table 4, for the experimental NMR chemical shifts for Rh complexes, see Table S3 in Supporting Information, for the DFT-calculated values, see Tables S4−S6 in Supporting Information).

The values in Table 5 demonstrate very good agreement between the experimental and theoretical ^{1}H and ^{13}C NMR data (for the statistical parameters and a short discussion, see Methods and Figures S1−S5 in Supporting Information). This allows for a detailed analysis of the paramagnetic NMR chemical shifts, which are generally determined by the contact contributions (δ^{con}) with the pseudocontact contributions (δ^{pc}) much less important, see Tables S4 and S5. As mentioned in the Introduction, the dominating δ^{con} is governed by the electronic structure and can be linked to the distribution of the spin density in the ligands. To demonstrate this phenomenon, we selected compound 8 with a 4-cyanophenyl substituent at the *para* position of the pyridine axial ligand.

Linking Paramagnetic Shift to Spin Density and Hyperfine Coupling Constant: A Case Study of Compound 8. We start our analysis by inspecting the paramagnetic ^{13}C NMR chemical shifts of the atoms of the phenyl ring more distant from the ruthenium center. It should be noted explicitly that the spin density in our complexes 1−8 is localized mainly in the *inter-bond* metal-based $4d_{xy}$ orbital found in the equatorial RuCl$_4$ plane (for the definition of the coordination system, see Section 3.5). Because the direct spin delocalization (related to the highest unpaired MSO) to distant atoms of the second phenyl ring is vanishingly small, spin polarization is the predominant mechanism affecting the paramagnetic NMR chemical shifts of the distant carbon atoms. This "indirect" effect is propagated to a great distance through π-space in the aromatic fragments.[78] The calculated spatial distribution of the spin density in the ligand moiety of compound 8 is shown in Figure 6a. Clearly, there is a qualitative correlation between the visualized α/β spin density in the
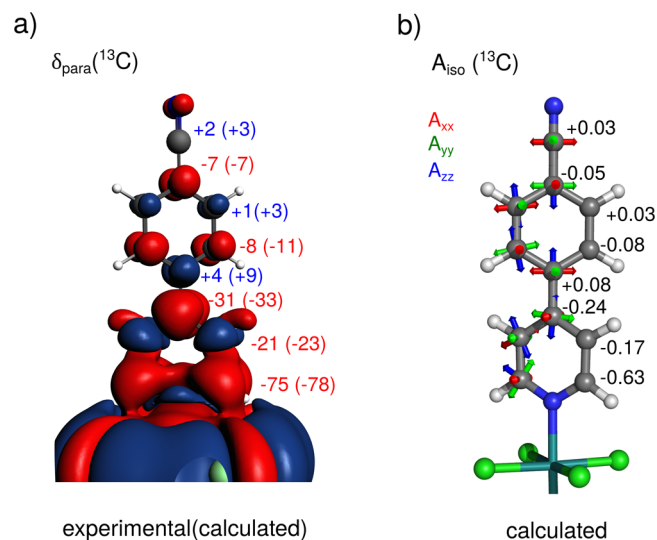

Figure 6. (a) Visualization of the 1c spin density (iso-surface at 0.00001 au), calculated by using the ZORA/PBE0/TZ2P/COSMO approach, and the experimental paramagnetic ^{13}C NMR chemical shifts (δ^{para}, the calculated values are shown in parentheses) for compound 8 at 293 K. The positive and negative values are shown in blue and red, respectively. (b) The calculated orientations of the principal components of the ^{13}C HF coupling tensors (A) and the isotropic ^{13}C HF coupling constants (A_{iso} in MHz), calculated at the SO-ZORA level (PBE0/TZ2P/COSMO). A_{xx} in red, A_{yy} in green, A_{zz} in blue. For the orientations of the principal components of the A(H2) coupling tensor, see Figure S8 in Supporting Information.

π-space of the individual carbon atoms of the phenyl ring (Figure 6a) and the signs of the experimental paramagnetic NMR chemical shifts (calculated values shown in parentheses). The alternation of the signs (Karplus-like dependence)[79,80] starting with C8 (−7 ppm), and going through C7 (+1 ppm), C6 (−8 ppm),

and C5 (+4 ppm) to C4 (−31 ppm) matches the pattern shown in Figure 6a.

However, for the carbon atoms of the pyridine ring found closer to the ruthenium center, other mechanisms of spin distribution involving σ-space start to play a role. Thus, C3 is significantly shielded by the paramagnetic contribution (δ^{para}) despite the positive value of the spin density in its π-subspace (blue lobe perpendicular to the aromatic ring in Figure 6a). For the C3 atom, the "indirect" deshielding (related to the positive polarization of π-space at the C3 atom) and somewhat stronger "quasi-direct" shielding (related to the negative polarization of the σ-space, the red lobe at the C2−C3 bond in Figure 6a) effects partially compensate each other, resulting in a net paramagnetic contribution δ^{para}(C3) = −21 ppm, which is significantly smaller than that of the more distant C4 (δ^{para} = −31 ppm). Note the opposite polarization of the π-space at atoms C3 and C4. The σ-space (quasi-direct) and π-space (indirect) negative polarization contributions for C2 (Figure 6a) add up to a sizable paramagnetic shielding δ^{para} = −75 ppm. For a more detailed description of the spin-polarization mechanism, see Section 3.5.

The paramagnetic ^{13}C NMR chemical shifts (δ^{para}) derive from the hyperfine coupling tensors (**A**) for the individual carbon atoms, see eqs 3 and 4 in Section 2: Methods. The alternating signs of the paramagnetic NMR chemical shifts discussed in the previous paragraphs originate in the alternating isotropic values of the ^{13}C hyperfine coupling constants (A_{iso}) shown in Figure 6b. Although the total A_{iso} values are determined by interplay between the Fermi-contact (FC), paramagnetic spin−orbit (PSO), and spin-dipolar (SD) contributions, the FC term is *the most structurally variable* for the carbon atoms of the ligands in complexes **1−8** (for examples of individual A terms for **2** and **3**, see Table S7 in Supporting Information).

It is clear from Table 5 that the NMR chemical shifts for the atoms of the pyridine ring are affected by the electronic character of the substituents (e.g., 4-Me vs 4-CN). As examples, the NMR chemical shifts and calculated **A**-tensors for the C3, C2, and H2 atoms as well as the differences between individual parameters for compounds **2** and **3** are summarized in Table S7 in Supporting Information. As discussed above, the contact contributions to the paramagnetic NMR chemical shifts derive from the corresponding A_{iso} (for a given g-value). For this reason, the A_{iso} values as well as the mechanism of spin distribution in the ligand and the effects of the solvent on the spin distribution are analyzed and discussed in detail in Section 3.5. However, we first analyze the nature of the bonding between the metal and the nitrogen atom, which is inevitably linked to the distribution of the spin density in the aromatic system of the ligand. To avoid any ambiguities related to the bonding analysis of a system containing an unpaired electron, we resorted to the diamagnetic rhodium analogs **3b** and **2b** as examples of the type, see Section 3.4.

3.4. Character of M−N Bonding: A Case Study of Diamagnetic Complexes 3b and 2b.

To analyze the bonding between the metal center and the nitrogen atom of the ligand in the rhodium analog **3b**, we used EDA analysis[34] as implemented in the ADF package. The total interaction energy −37.5 kcal mol^{-1} is broken down into the electrostatic (−103.6 kcal mol^{-1}), Pauli repulsion (+116.7 kcal mol^{-1}), and orbital (−50.7 kcal mol^{-1}) terms. Further, the orbital term can be linked to the individual contributions made by natural orbitals for chemical valence (NOCV)[81,82] to the electron deformation density (EDD).

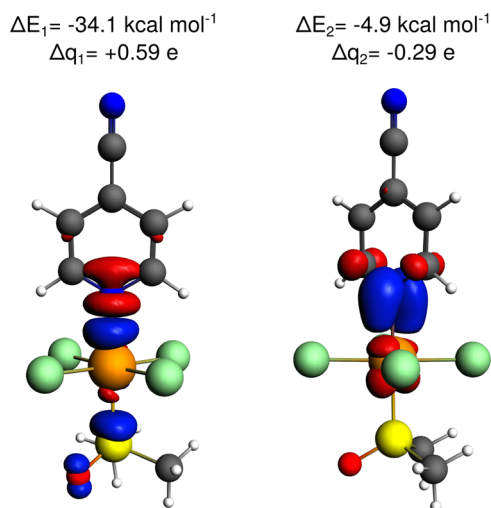The two most important EDA-NOCV channels for the M−N bond in **3b** are shown in Figure 7. The first NOCV

ΔE_1 = -34.1 kcal mol^{-1} ΔE_2 = -4.9 kcal mol^{-1}
Δq_1 = +0.59 e Δq_2 = -0.29 e

Figure 7. Two most important NOCV channels for the M−N bond in compound **3b** with the corresponding contributions to the EDA orbital term and the charge transfer calculated at the ZORA level (PBE0/TZ2P). The values 0.003 au and 0.001 au were used to plot the iso-surface of the first (left) and second (right) channel, respectively. The corresponding values for compound **2b** (not shown): E_1 = −35.5 kcal mol^{-1}, E_2 = −4.4 kcal mol^{-1}, Δq_1 = +0.61 e, Δq_2 = −0.25 e.

channel (ΔE_1 = −34.1 kcal mol^{-1}) represents the donation of the lone pair of electrons of the nitrogen atom to the metal center (σ-bonding).[83] The π-back bonding with the charge transfer from the metal d atomic orbital (AO) to nitrogen p AO (ΔE_2 = −4.9 kcal mol^{-1}) is shown as the second channel in Figure 7. Comparing the M−N bonding NOCV characteristics of **2b** and **3b**, the electron-rich aromatic ring in the Me derivative (**2b**) enables the lone pair of electrons at the nitrogen atom to interact slightly more efficiently with the metal center (ΔE_1 = −35.5 kcal mol^{-1}) compared to that in **3b** (ΔE_1 = −34.1 kcal mol^{-1}). However, π-back-donation is seen to be somewhat more efficient for compound **3b** (ΔE_2 = −4.9 kcal mol^{-1}) compared to that for **2b** (ΔE_2 = −4.4 kcal mol^{-1}) because of the strong π-electron accepting properties of the CN group. Because the complexes being investigated are negatively charged (the total charge is −1), the delocalization of electrons from the negatively charged M$^{\text{III}}$Cl$_4$ unit to the ligand moiety is more efficient in the CN derivative **3b**.

The above-mentioned σ- and π-bonding interactions are important for the mechanism and magnitude of the spin distribution in the aromatic ligands of paramagnetic ruthenium complexes. The ^{1}H and ^{13}C pNMR and A_{iso} values for **2** and **3** (see Table S7) can be linked to the characteristics of the Ru−N bond as well as to the direct substituent electronic effects on the individual atoms of the ligand, as discussed in detail in Section 3.5.

3.5. Spin Polarization: Mechanism, Electronic and Solvent Effects. *Spatial Distribution of Spin Density: A Case Study of Compound 3.*

The very good agreement between the experimental and calculated NMR chemical shifts, discussed in Section 3.3, and the M−N bonding characteristics described in Section 3.4, enable a more detailed analysis of the electronic and solvent effects on the NMR chemical shifts. However, as the contact contributions (δ^{con}) to the paramagnetic NMR chemical shifts are linked directly to the isotropic hyperfine coupling constants, A_{iso}, see eq 3, we focus our analysis and discussion on the total A_{iso} or $A_{\text{iso}}^{\text{FC}}$ values and their link to the spatial distribution of the spin density. We first visualize the

spatial distribution of the one-component (1c) spin density in compound **3** for several iso-surface values, using Figure 8 as an example.
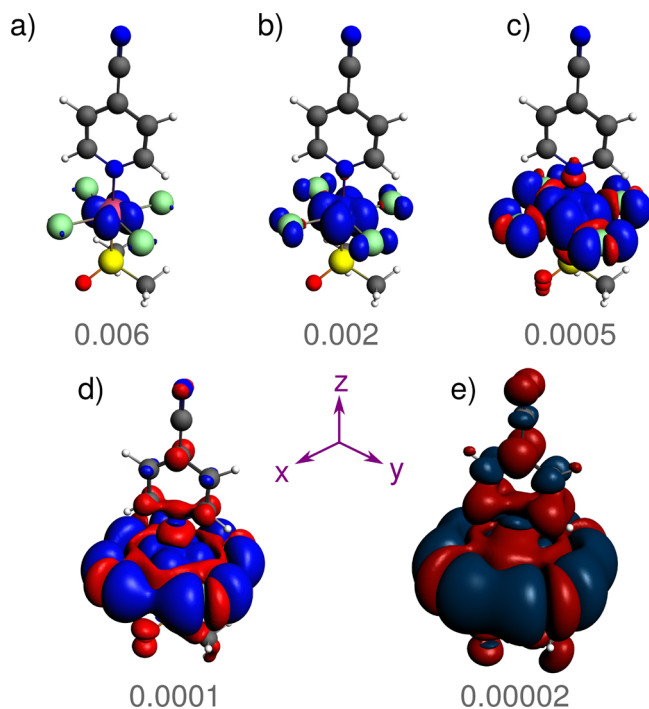

Figure 8. A visualization of the 1c spin density in compound **3** for isovalues (a) 0.006 au, (b) 0.002 au, (c) 0.0005 au, (d) 0.0001 au, and (e) 0.00002 au, calculated at the ZORA level (PBE0/TZP/COSMO). For visualization of the z-component of the 4c spin density, see Figure S9 in Supporting Information.

As mentioned in Section 3.3, the spin density in complex **3** resides mainly in the *inter-bond* metal-based $4d_{xy}$ orbital found in the equatorial $RuCl_4$ plane (Figure 8a, 0.006 au). The spin density is partly delocalized to the lone pairs of electrons of the chlorine atoms in the equatorial plane (blue lobes in Figure 8b, 0.002 au). This is related to the in-plane Ru−Cl π-antibonding (π^*) character of the corresponding orbital (composed of a ruthenium $4d_{xy}$ atomic orbital (AO) and the in-plane chlorine p_π AOs, see Table S8 in Supporting Information). However, as expected for reasons of symmetry, the direct spin delocalization in this molecular spin−orbital to the axial ligands is vanishingly small (see below). Therefore, the propagation of the spin density to the aromatic pyridine moiety includes several spin-polarization steps.[78,84,85] This spin polarization is clearly visible for the Ru−Cl, Ru−N, and Ru−S σ-bonds, as shown in Figure 8c (red lobes). The spin polarization toward the pyridine moiety (Ru−N bond) is particularly important for our discussion. An imbalance in the spin density found close to the nitrogen atom of the ligand (negative $\rho^{\alpha-\beta}$) is further delocalized to C2 (cf. quasi-direct propagation in σ-space in Section 3.3) in the aromatic plane and also, to a lesser extent, to C3 via the σ_{C-C} bonding region (Figure 8d and 8e). In parallel, the spin-polarization mechanism in the aromatic system generates spin density in p_π-space (perpendicular to the aromatic plane, Figure 8e; cf. indirect spin-polarization effects in Section 3.3.), with the corresponding spin populations for the individual carbon atoms (see below).

Molecular Spin−Orbital (MSO) Contributions to the A_{iso} and MSO Spin-Density: A Case Study of the Mechanism for H-2 in Compound 3. The above-mentioned qualitative

description of the mechanism of distribution of the spin-density from the ruthenium center to the ligand atoms can be linked to the spatial distribution of spin-density in the MSOs and qualitatively also to the contributions of the molecular spin−orbitals (MSOs) to the isotropic hyperfine coupling constants (A_{iso}) substantiated by the predominance of *the most structurally variable* A_{iso}^{FC} contribution to A_{iso}^{tot} (Table S7; the quantitative correlation could be performed for A_{iso}^{FC} values). The MSO analysis discussed in this section was performed at the 4c level *in vacuo*. The contributions of MSOs that differ in energy by less than 0.27 eV have been summed up (after inspecting the overlap criteria) to form MSO pairs.[86,87] Because the vector of spin density calculated at the 4c level can hardly be interpreted using standard chemical concepts (and the Fermi-contact contribution to the A_{iso} is generally highly isotropic), we visualize and interpret the z-component of the spin-density for the individual MSOs. The spin densities (z-components) of the 4c MSOs with the most significant contributions to the $A_{iso}(H2)$ value (denoted as *A*-active) together with the MSO energies and the A_{iso}-contributions are shown in Figure 9 (for one-component orbitals, see Table S8 in Supporting Information).
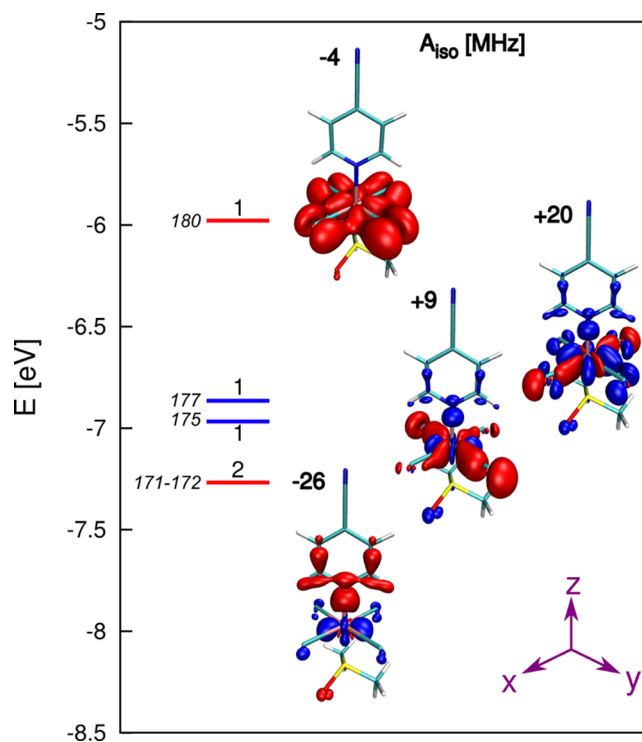

Figure 9. Visualization of the z-component of the 4c spin density for the most important individual or summed $A_{iso}(H2)$-active MSOs, MSOs energies, and the A_{iso}^{total} (H2) contributions of MSOs for compound **3**. The negative and positive z-component of the spin density calculated at the 4c relativistic level (DKS) are shown in red and blue, respectively.

As demonstrated in the previous part of this section, the spin density resides mainly in the equatorial *inter-bond* metal-based MSO (MSO 205, π-antibonding Ru−Cl character in Table S8, cf. the spin density in Figure 8a). The spin density is delocalized to the lone pairs of electrons (LP) of the chlorine atoms (Figure 9), as also mentioned in the qualitative outline of the spin delocalization/polarization mechanism based on the total distribution of the spin-density in Figure 8. However, the contributions of the hydrogen/carbon AOs of the pyridine ring in

the MSO 205 are negligible as reflected by the vanishingly small spin delocalization to these atoms and, consequently, a negligible MSO-205 contribution to the ligand hyperfine coupling constants. As a result of the spin delocalization to the chlorines, these atoms play a significant role in the spin-polarization contributions. Therefore, MSO 180 with significant contributions from the Cl lone pairs can be considered to be spin-polarized at the chlorine atoms as evidenced by its negative spin-density in the equatorial plane and negative contribution to the $A_{iso}(H2)$, Figure 9. Its rather limited contribution to the $A_{iso}(H2)$, however, corresponds to the small AO contribution of H2 in this MSO. MSOs 177 and 175 also have significant contributions from the in-plane ruthenium-based d AOs. Despite the negative spin density in $\sigma(Ru-Cl)$ space, they have a positive character in $\sigma(Ru-N)$ space and, importantly, also in the position of the H2 atom (and C2, C3). As expected, in parallel with the decreasing energy of these MSOs and the increasing contributions of hydrogen/carbon AOs, their contributions to $A_{iso}(H2)$ are increasing. In contrast to MSOs 177 and 175, the σ-space for the MSO pair 171−172 is highly negatively spin-polarized in the regions of the Ru−N, C−C, and C−H bonds (see Figure 9).

Although both the $\sigma_{N\to Ru}$ donation (1st channel in Figure 7) and $\pi_{Ru\to N}$ back-donation (2nd channel in Figure 7) interactions have been discussed in Section 3.4., the σ_{Ru-N} bonding seems to play a more important role in $A_{iso}(H2)$-active MSOs (see previous paragraph). However, the $\pi_{Ru\to N}$ back-donation can play a significant role in the spin-polarization mechanism despite its negligible direct effects on the ^1H and ^{13}C hyperfine coupling constants (in analogy to the FC mechanism of indirect nuclear spin−spin coupling constants[88]). Contributions to $A_{iso}(H2)$ from the lower-lying MSOs are less important or compensate each other in the pairs.

In total, the individual MSO contributions (summing up the A_{iso}^{FC}, A_{iso}^{PSO}, and A_{iso}^{SD} terms) mutually compensate each other leaving the net $A_{iso}(H2)$ values for complexes 1−8 smaller than 1 MHz, e.g., see Table S7. However, subtle imbalances in the distribution of the spin density still have significant effects on the ^1H and ^{13}C NMR chemical shifts. Only the delicate imbalances between the various quasi-direct (σ-space) and indirect (π-space) spin-polarization contributions determine the sign and magnitude of the principal components of the A-tensors and the A_{iso} values for the ^1H and ^{13}C atoms in complexes 1−8. The δ_{iso}^{para} and A_{iso} modulations caused by electronic and solvent effects are discussed in the following subsections.

Electron and Spin Densities in the Pyridine Ligand for the Series of Compounds 1−3: Substituent Effects on the Paramagnetic NMR Chemical Shifts. The mechanism of spin distribution discussed in the previous sections can be extended to all the atoms of the aromatic ligand. However, particularly interesting are the trends in individual ^{13}C NMR chemical shifts for the series of compounds 1−3 (complexes with different electron donating/accepting properties of R). As the C4 NMR chemical shifts are significantly affected by the direct *ipso*-bound 4-R substituents (σ/π-donor/acceptor), we focus our analysis on C2 and C3. The first step is to correlate δ^{para} with the atomic Hirschfeld charges, see Figure 10a.

As expected, the CN group in compound 3 (in blue) attracts the electron density, causing a significant decrease in the negative charges on the C2 and C3 atoms compared to those atoms in compounds 1 (in green) and 2 (in red). Although this electron-pulling effect of the CN group leads to a larger negative $\delta^{para}(C2)$, the opposite trend is identified for $\delta^{para}(C3)$, see Figure 10a. The electron-acceptor group CN with a polarizable

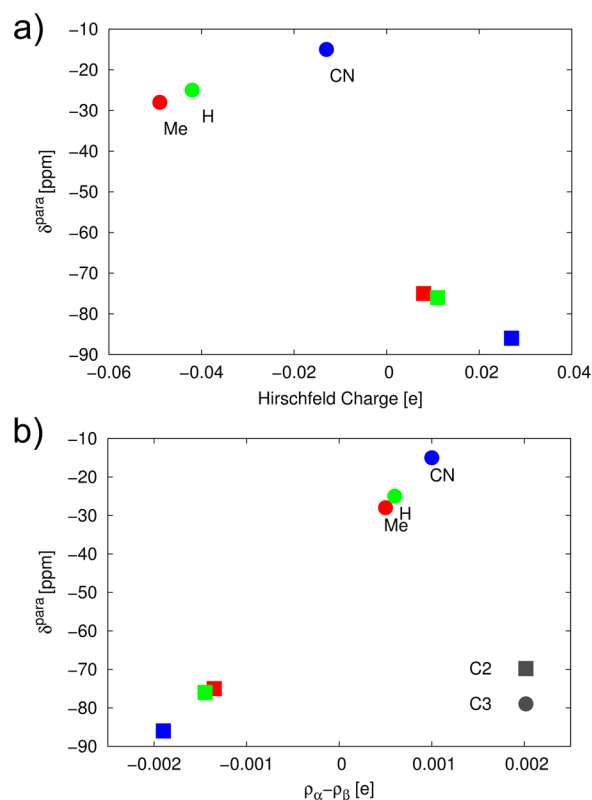**Figure 10.** Dependence of the paramagnetic ^{13}C NMR chemical shift ($\delta^{para} = \delta^{con} + \delta^{pc}$) on (a) the Hirschfeld charge of each particular atom, (b) the 1c spin population in the p-AOs ($\rho_p^{\alpha-\beta}$) of each particular atom. The data for atoms C2 (squares) and C3 (circles) in compounds 1 (H in green), 2 (Me in red), and 3 (CN in blue) are shown for the temperature 293 K.

π-space thus amplifies the differences between C2 and C3, which must originate in a larger spin-polarization in the aromatic ligand. This effect is analogous to the well-known increase in indirect nuclear spin−spin interactions in the presence of electron-acceptor groups or polarizable molecular fragments (e.g., lone pairs of electrons, neighboring π bonds).[89,88] The spin-polarization enhancement by the CN group is qualitatively visualized in the spatial distribution of the 1c spin density shown in Figure 11 (compare 2 and 3) and quantitatively demonstrated by correlating $\delta^{para}(^{13}C)$ with the 1c spin population in the carbon p-type AOs ($\rho_p^{\alpha-\beta}$) in Figure 10b. As assumed, the larger spin polarization in compound 3 (compared to 1 and 2) gives a larger δ^{para} (1c $\rho_p^{\alpha-\beta} < 0$) for C2 but a smaller δ^{para} (1c $\rho_p^{\alpha-\beta} > 0$) for C3. The reverse trend for C3 originates in the balance between the "quasi-direct" (σ-space) and "indirect" (π-space) spin-polarization effects discussed in Section 3.3.

Solvent Effects: NMR Parameters at Experimental Conditions. To investigate the effects of the solvent on the paramagnetic ^{13}C NMR chemical shifts, we performed the SO-ZORA calculations *in vacuo* as well as using the COSMO model of dimethylformamide (the solvent used in the NMR experiments). The SO-ZORA calculated δ^{para} values for compounds 2 and 3 are summarized in Table 5 and the contact contributions to the NMR chemical shifts (δ^{con}) are schematically compared to the 1c spin-density distribution in Figure 11. It should be mentioned that the effects of the solvent on the pseudocontact contributions to the NMR chemical shifts (δ^{pc}) are rather marginal. Clearly, the effect of the solvent on the δ^{con} is predominant (Table S4, S5 in Supporting Information).
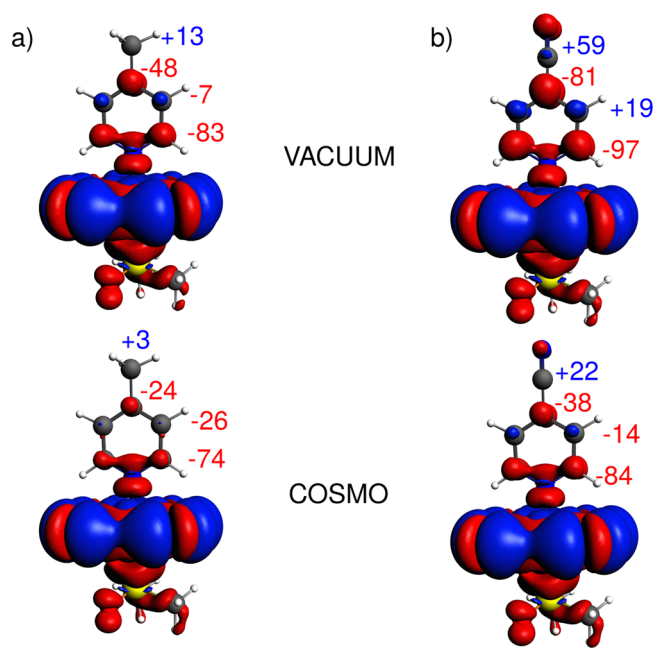
Figure 11. Visualization of the 1c spin density (iso-surface at 0.0001 au) and contact contributions to the paramagnetic ^{13}C NMR chemical shifts (δ^{con}) at 293 K for (a) compound **2** and (b) compound **3**, calculated *in vacuo* (top) and using the COSMO model of dimethylformamide solvent (bottom).

For example, it changes δ^{con} for C4 in compound **3** from -81 ppm *in vacuo* to -38 ppm in COSMO. The analogous shielding effect of the solvent switches the deshielding $\delta^{con} = +19$ ppm (*in vacuo*) to the shielding $\delta^{con} = -14$ ppm (in COSMO) for C3 in compound **3**. As the δ^{con} can be linked directly to the dominating and variable A_{iso}^{FC}, it is essential to include a solvent in the calculation of the EPR parameters (**A**-tensor, **g**-tensor)[90−92] and it should be used in all studies aimed at reproducing or predicting the magnetic resonance parameters under experimental conditions.

4. CONCLUSIONS

In this contribution, a systematic study of the ^{1}H and ^{13}C NMR chemical shifts, δ, in a series of designed and prepared pyridine-based Ru^{III} complexes was performed. The experimental NMR chemical shifts and their orbital (temperature-independent) and paramagnetic (temperature-dependent) contributions were estimated from 1D NMR spectra measured in the temperature range 233−323 K and analyzed using Curie plots (δ as a function of $1/T$). The orbital contributions to δ for the individual atoms in the ruthenium complexes were compared with the total NMR chemical shifts in diamagnetic Rh^{III} analogs. The paramagnetic contributions (δ^{con} and δ^{pc}) to the ^{1}H and ^{13}C NMR chemical shifts were calculated relative to the structural variability of the EPR hyperfine coupling constants (A_{iso}), and qualitatively linked to the spatial distribution of spin density in the ruthenium complexes.

The contributions to selected A_{iso} values from the molecular spin−orbitals (MSOs) were analyzed at the four-component relativistic DFT level and were demonstrated for A_{iso}(H2), as an example. The direct contribution to δ^{con}(H2) and A_{iso}(H2) from the highest unpaired MSO of the Ru−Cl π-antibonding nature is vanishingly small because of the very weak direct spin delocalization from the ruthenium center to the aromatic heterocycle. However, it affects the lower-lying MSOs of the Ru−Cl

π-bonding character. These MSOs contain greater contributions from the ligand AOs (including H2) and contribute negatively to A_{iso}(H2). In contrast, the MSOs which have more of a Ru−Cl σ-bonding character (with notable coefficients of the ligand AOs) contribute positively to the A_{iso}(H2). The third important (negative) contribution to A_{iso}(H2) is linked to the significantly spin-polarized pair of MSOs involving Ru−N σ-bonding of the pyridine ligand as well as the carbon and hydrogen AOs of the ligand. This spin-polarized density is "quasi-directly" delocalized to the C2, C3, and H2 atoms via the σ-space. A balance between the "quasi-direct" (σ-space) and "indirect" (π-space) polarization contributions to A_{iso} for several ligand atoms has been analyzed and discussed.

On the basis of the results achieved, several conclusions can be drawn.

(i) The error in extracting the δ^{para} and δ^{orb} contributions from the experimental temperature-dependent NMR spectra is estimated to be ± 0.2 ppm for ^{1}H and ± 1 ppm for ^{13}C. However, for atoms close to the ruthenium paramagnetic center, the deviation can amount to ± 1 ppm and ± 5 ppm for ^{1}H and ^{13}C, respectively.

(ii) Relativity does not play a very significant role in the paramagnetic ^{1}H NMR chemical shift calculations for the Ru(III) complexes investigated in this work. In contrast, this effect seems quite important for the paramagnetic ^{13}C NMR chemical shifts; the two-component DFT approach including the solvent model selected in this work provides reliable data. The estimated relative importance of the individual physical effects on the calculated paramagnetic ^{1}H NMR chemical shifts of the H2 atom decreases in the order: solvent ($\sim$8 ppm) > relativity ($\sim$3 ppm) $\approx$ exact-exchange (EE) admixture ($\sim$2 ppm) > ion ($\sim$1 ppm). However, the effects of relativity and the amount of the EE admixture in the PBE0 functional are more important for the paramagnetic ^{13}C NMR chemical shifts; for C2: EE admixture ($\sim$60 ppm) > solvent ($\sim$30 ppm) $\approx$ relativity ($\sim$20 ppm) > ion ($\sim$2 ppm). The solvent effects should be included (at least implicitly) in all calculations that aim to reproduce or predict the experimental paramagnetic NMR data.

(iii) The magnitudes and signs of the paramagnetic contributions to the NMR chemical shifts of the individual ^{13}C atoms of the pyridine-based ligand can be rationalized by inspecting the spatial distribution of the spin density as well as analyzing the contributions from the molecular spin−orbitals to the hyperfine coupling constants. The A_{iso} values can be interpreted as a result of interplay between the various spin-polarization contributions. The delicate balance between the positive and negative MSO contributions results in small total A_{iso} values. However, these small A_{iso} values still have a significant effect on the ^{1}H and ^{13}C NMR spectra. The substituent-induced effects on the paramagnetic ^{13}C NMR chemical shifts can be linked to atomic charges at individual atoms and the spin populations in p atomic orbitals.

The systematic methodological study of the NMR chemical shifts presented in this work should contribute to our understanding of the factors influencing the distribution of spin density in transition-metal complexes that is generally responsible for the paramagnetic contribution to the NMR shifts, and to stimulate further combined experimental-theoretical investigations of open-shell systems including metallodrugs.

■ ASSOCIATED CONTENT

⑤ Supporting Information

The Supporting Information is available free of charge on the ACS Publications website at DOI: 10.1021/jacs.6b02749.

> Methods, experimental and calculated NMR data, additional figures, Cartesian coordinates and energies (PDF)
>
> Additional crystal structure data for compounds **3**, **4**, **7**, **2b**, **3b**, and **4b** (CIF)

■ AUTHOR INFORMATION

Corresponding Author

*rmarek@chemi.muni.cz

Notes

The authors declare no competing financial interest.

■ ACKNOWLEDGMENTS

■ REFERENCES

(1) Rosenberg, B.; Vancamp, L.; Krigas, T. *Nature* **1965**, *205*, 698–699.

(2) Reedijk, J. *Proc. Natl. Acad. Sci. U. S. A.* **2003**, *100* (7), 3611–3616.

(3) Levina, A.; Mitra, A.; Lay, P. A. *Met. Integr. Biometal Sci.* **2009**, *1* (6), 458–470.

(4) Han Ang, W.; Dyson, P. J. *Eur. J. Inorg. Chem.* **2006**, *2006* (20), 4003–4018.

(5) Ang, W. H. *Chimia* **2007**, *61* (4), 140–142.

(6) Mestroni, G.; Alessio, E.; Sava, G.; Pacor, S.; Coluccia, M.; Boccarelli, A. *Met.-Based Drugs* **1994**, *1* (1), 41–63.

(7) Groessl, M.; Reisner, E.; Hartinger, C. G.; Eichinger, R.; Semenova, O.; Timerbaev, A. R.; Jakupec, M. A.; Arion, V. B.; Keppler, B. K. *J. Med. Chem.* **2007**, *50* (9), 2185–2193.

(8) Scolaro, C.; Bergamo, A.; Brescacin, L.; Delfino, R.; Cocchietto, M.; Laurenczy, G.; Geldbach, T. J.; Sava, G.; Dyson, P. J. *J. Med. Chem.* **2005**, *48* (12), 4161–4171.

(9) Rademaker-Lakhai, J. M.; Bongard, D.; van den Pluim, D.; Beijnen, J. H.; Schellens, J. H. M. *Clin. Cancer Res.* **2004**, *10* (11), 3717–3727.

(10) Leijen, S.; Burgers, S. A.; Baas, P.; Pluim, D.; Tibben, M.; van Werkhoven, E.; Alessio, E.; Sava, G.; Beijnen, J. H.; Schellens, J. H. M. *Invest. New Drugs* **2015**, *33* (1), 201–214.

(11) Bacac, M.; Hotze, A. C.; Schilden, K.; van der Haasnoot, J. G.; Pacor, S.; Alessio, E.; Sava, G.; Reedijk, J. *J. Inorg. Biochem.* **2004**, *98* (2), 402–412.

(12) Clarke, M. J. *Coord. Chem. Rev.* **2003**, *236* (1–2), 209–233.

(13) La Mar, G. N.; DeW Horrocks, W.; Holm, R. H. *NMR of Paramagnetic Molecules*; Academic Press: New York, 1973; p 694.

(14) In *NMR of Paramagnetic Molecules*; Berliner, L. J., Reuben, J., Eds.; Springer US: Boston, MA, 1993; Biological Magnetic Resonance, Vol. *12*.

(15) Bertini, I.; Luchinat, C.; Aime, S. *Coord. Chem. Rev.* **1996**, *150*, R7.

(16) Bertini, I.; Luchinat, C.; Parigi, G. *Solution NMR of Paramagnetic Molecules: Applications to Metallobiomolecules and Models*; Elsevier: Amsterdam, 2001; p 384.

(17) Shokhirev, N. V.; Walker, F. A. *J. Phys. Chem.* **1995**, *99* (50), 17795–17804.

(18) Banci, L.; Bertini, I.; Luchinat, C.; Pierattelli, R.; Shokhirev, N. V.; Walker, F. A. *J. Am. Chem. Soc.* **1998**, *120* (33), 8472–8479.

(19) Neese, F. In *Calculation of NMR and EPR Parameters*; Kaupp, M., Bühl, M., Malkin, V., Eds.; Wiley-VCH Verlag, 2004; pp 541–564.

(20) Kurland, R. J.; McGarvey, B. R. *J. Magn. Reson.* **1970**, *2* (3), 286–301.

(21) Martin, B.; Autschbach, J. *J. Chem. Phys.* **2015**, *142* (5), 54108.

(22) Heuvel, W. V. d.; Soncini, A. *J. Chem. Phys.* **2013**, *138* (5), 54113.

(23) Moon, S.; Patchkovskii, S. In *Calculation of NMR and EPR Parameters*; Kaupp, M., Bühl, M., Malkin, V., Eds.; Wiley-VCH Verlag, 2004; pp 325–338.

(24) Van den Heuvel, W.; Soncini, A. *Phys. Rev. Lett.* **2012**, *109* (7), 73001.

(25) Gendron, F.; Sharkas, K.; Autschbach, J. *J. Phys. Chem. Lett.* **2015**, *6* (12), 2183–2188.

(26) Vaara, J.; Rouf, S. A.; Mareš, J. *J. Chem. Theory Comput.* **2015**, *11* (10), 4840–4849.

(27) Rouf, S. A.; Mareš, J.; Vaara, J. *J. Chem. Theory Comput.* **2015**, *11* (4), 1683–1691.

(28) Autschbach, J.; Patchkovskii, S.; Pritchard, B. *J. Chem. Theory Comput.* **2011**, *7* (7), 2175–2188.

(29) Rastrelli, F.; Bagno, A. *Chem. - Eur. J.* **2009**, *15* (32), 7990–8004.

(30) Rastrelli, F.; Bagno, A. *Magn. Reson. Chem.* **2010**, *48*, S132–141.

(31) Aquino, F.; Pritchard, B.; Autschbach, J. *J. Chem. Theory Comput.* **2012**, *8* (2), 598–609.

(32) Komorovsky, S.; Repisky, M.; Ruud, K.; Malkina, O. L.; Malkin, V. G. *J. Phys. Chem. A* **2013**, *117* (51), 14209–14219.

(33) Autschbach, J. In *Annual Reports in Computational Chemistry*; Dixon, D. A., Ed.; Elsevier, 2015; Vol. *11*, pp 3–36.

(34) te Velde, G.; Bickelhaupt, F. M.; Baerends, E. J.; Fonseca Guerra, C.; van Gisbergen, S. J. A.; Snijders, J. G.; Ziegler, T. *J. Comput. Chem.* **2001**, *22* (9), 931–967.

(35) *ReSpect, Relativistic Spectroscopy DFT Program*, version 3.4.2; 2015; Repisky, M.; Komorovsky, S.; Malkin, V. G.; Malkina, O. L.; Kaupp, M.; Ruud, K.; Bast, R.; Ekstrom, U.; Knecht, S.; Malkin Ondik, I.; Malkin, E. http://www.respectprogram.org.

(36) Alessio, E.; Balducci, G.; Calligaris, M.; Costa, G.; Attia, W. M.; Mestroni, G. *Inorg. Chem.* **1991**, *30* (4), 609–618.

(37) Henbest, H. B.; Trocha-Grimshaw, J. *J. Chem. Soc., Perkin Trans. 1* **1974**, 607–608.

(38) Pavlovic, V.; Petkovic, M.; Popovic, S.; Savic, V. *Synth. Commun.* **2009**, *39* (23), 4249–4263.

(39) Webb, M. I.; Chard, R. A.; Al-Jobory, Y. M.; Jones, M. R.; Wong, E. W. Y.; Walsby, C. J. *Inorg. Chem.* **2012**, *51* (2), 954–966.

(40) Sheldrick, G. M. *Acta Crystallogr., Sect. A: Found. Crystallogr.* **2008**, *64* (1), 112–122.

(41) Bax, A.; Summers, M. F. *J. Am. Chem. Soc.* **1986**, *108* (8), 2093–2094.

(42) Adamo, C.; Barone, V. *J. Chem. Phys.* **1999**, *110* (13), 6158–6170.

(43) Adamo, C.; Scuseria, G. E.; Barone, V. *J. Chem. Phys.* **1999**, *111* (7), 2889–2899.

(44) Schäfer, A.; Huber, C.; Ahlrichs, R. *J. Chem. Phys.* **1994**, *100* (8), 5829–5835.

(45) Andrae, D.; Häußermann, U.; Dolg, M.; Stoll, H.; Preuß, H. *Theor. Chim. Acta* **1990**, *77* (2), 123–141.

(46) TURBOMOLE V6.2 2010; TURBOMOLE GmbH: 2007; http://www.turbomole.com.

(47) Klamt, A.; Schüürmann, G. J. Chem. Soc., Perkin Trans. 2 1993, 799−805.

(48) Vicha, J.; Patzschke, M.; Marek, R. Phys. Chem. Chem. Phys. 2013, 15 (20), 7740−7754.

(49) Vícha, J.; Novotný, J.; Straka, M.; Repisky, M.; Ruud, K.; Komorovsky, S.; Marek, R. Phys. Chem. Chem. Phys. 2015, 17 (38), 24944−24955.

(50) Standara, S.; Maliňáková, K.; Marek, R.; Marek, J.; Hocek, M.; Vaara, J.; Straka, M. Phys. Chem. Chem. Phys. 2010, 12 (19), 5126−5139.

(51) Standara, S.; Bouzková, K.; Straka, M.; Zacharová, Z.; Hocek, M.; Marek, J.; Marek, R. Phys. Chem. Chem. Phys. 2011, 13 (35), 15854−15864.

(52) Pawlak, T.; Munzarová, M. L.; Pazderski, L.; Marek, R. J. Chem. Theory Comput. 2011, 7 (12), 3909−3923.

(53) ADF2014, SCM, Theoretical Chemistry; Vrije Universiteit: Amsterdam, The Netherlands; http://www.scm.com.

(54) Lenthe, E. v.; Snijders, J. G.; Baerends, E. J. J. Chem. Phys. 1996, 105 (15), 6505−6516.

(55) Saue, T. ChemPhysChem 2011, 12 (17), 3077−3094.

(56) Perdew, J. P.; Burke, K.; Ernzerhof, M. Phys. Rev. Lett. 1996, 77 (18), 3865−3868.

(57) Adamo, C.; Barone, V. Chem. Phys. Lett. 1998, 298 (1−3), 113−119.

(58) Güell, M.; Luis, J. M.; Solà, M.; Swart, M. J. Phys. Chem. A 2008, 112 (28), 6384−6391.

(59) Eschrig, H.; Servedio, V. D. P. J. Comput. Chem. 1999, 20 (1), 23−30.

(60) Cohen, A. J.; Mori-Sánchez, P.; Yang, W. Chem. Rev. 2012, 112 (1), 289−320.

(61) Pritchard, B.; Autschbach, J. Inorg. Chem. 2012, 51 (15), 8340−8351.

(62) Martin, B.; Autschbach, J. Phys. Chem. Chem. Phys. 2016, DOI: 10.1039/C5CP07667F.

(63) Repisky, M.; Komorovsky, S.; Malkin, E.; Malkina, O. L.; Malkin, V. G. Chem. Phys. Lett. 2010, 488 (1), 94−97.

(64) Malkin, E.; Repisky, M.; Komorovsky, S.; Mach, P.; Malkina, O. L.; Malkin, V. G. J. Chem. Phys. 2011, 134 (4), 44111.

(65) Gohr, S.; Hrobárik, P.; Repisky, M.; Komorovsky, S.; Ruud, K.; Kaupp, M. J. Phys. Chem. A 2015, 119 (51), 12892−12905.

(66) Jensen, F. J. Chem. Theory Comput. 2006, 2 (5), 1360−1369.

(67) Dyall, K. G. Theor. Chem. Acc. 2007, 117 (4), 483−489.

(68) Webb, M. I.; Wu, B.; Jang, T.; Chard, R. A.; Wong, E. W. Y.; Wong, M. Q.; Yapp, D. T. T.; Walsby, C. J. Chem. - Eur. J. 2013, 19 (50), 17031−17042.

(69) Silvano Geremia, E. A. Inorg. Chim. Acta 1996, 253 (1), 87−90.

(70) Paula, Q. A. de; Batista, A. A.; Nascimento, O. R.; Costa-Filho, A. J. da; Schultz, M. S.; Bonfadini, M. R.; Oliva, G. J. Braz. Chem. Soc. 2000, 11 (5), 530−536.

(71) Griffith, D.; Cecco, S.; Zangrando, E.; Bergamo, A.; Sava, G.; Marmion, C. J. JBIC, J. Biol. Inorg. Chem. 2008, 13 (4), 511−520.

(72) Bühl, M.; Kabrede, H. J. Chem. Theory Comput. 2006, 2 (5), 1282−1290.

(73) Bühl, M.; Reimann, C.; Pantazis, D. A.; Bredow, T.; Neese, F. J. Chem. Theory Comput. 2008, 4 (9), 1449−1459.

(74) Martin, G. E.; Crouch, R. C. J. Nat. Prod. 1991, 54 (1), 1−70.

(75) Martin, G. E.; Zektzer, A. S. Two Dimensional NMR Methods for Establishing Molecular Connectivity; Wiley-VCH, 1988.

(76) Marek, R.; Lycka, A. Curr. Org. Chem. 2002, 6 (1), 35−66.

(77) Marek, R.; Lycka, A.; Kolehmainen, E.; Sievanen, E.; Tousek, J. Curr. Org. Chem. 2007, 11 (13), 1154−1205.

(78) Cano, J.; Ruiz, E.; Alvarez, S.; Verdaguer, M. Comments Inorg. Chem. 1998, 20 (1), 27−56.

(79) Karplus, M. J. Chem. Phys. 1959, 30 (1), 11−15.

(80) Karplus, M. J. Am. Chem. Soc. 1963, 85 (18), 2870−2871.

(81) Mitoraj, M. P.; Michalak, A.; Ziegler, T. J. Chem. Theory Comput. 2009, 5 (4), 962−975.

(82) Mitoraj, M. P.; Parafiniuk, M.; Srebro, M.; Handzlik, M.; Buczek, A.; Michalak, A. J. Mol. Model. 2011, 17 (9), 2337−2352.

(83) Mitoraj, M. P.; Zhu, H.; Michalak, A.; Ziegler, T. Int. J. Quantum Chem. 2009, 109 (14), 3379−3386.

(84) Munzarová, M. L.; Kubáček, P.; Kaupp, M. J. Am. Chem. Soc. 2000, 122 (48), 11900−11913.

(85) Munzarová, M. L. In Comprehensive Inorganic Chemistry II, 2nd ed.; Elsevier: Amsterdam, 2013; pp 359−380.

(86) Remenyi, C.; Kaupp, M. J. Am. Chem. Soc. 2005, 127 (32), 11399−11413.

(87) Kaupp, M.; Asher, J.; Arbuznikov, A.; Patrakov, A. Phys. Chem. Chem. Phys. 2002, 4 (22), 5458−5466.

(88) Marek, R.; Křístková, A.; Maliňáková, K.; Toušek, J.; Marek, J.; Hocek, M.; Malkina, O. L.; Malkin, V. G. J. Phys. Chem. A 2010, 114 (24), 6689−6700.

(89) Contreras, R. H.; Peralta, J. E. Prog. Nucl. Magn. Reson. Spectrosc. 2000, 37 (4), 321−425.

(90) Straka, M.; Kaupp, M.; Roduner, E. Theor. Chem. Acc. 2005, 114 (4−5), 318−326.

(91) Neugebauer, J.; Louwerse, M. J.; Belanzoni, P.; Wesolowski, T. A.; Baerends, E. J. J. Chem. Phys. 2005, 123 (11), 114101.

(92) Pavone, M.; Benzi, C.; De Angelis, F.; Barone, V. Chem. Phys. Lett. 2004, 395 (1−3), 120−126.